Hyperelastic phase-field fracture mechanics modeling of the toughening induced by Bouligand structures in natural materials

Sheng Yin[a], Wen Yang[b], Junpyo Kwon[c], Amy Wat[a], Marc A. Meyers[b,d], Robert O. Ritchie[a,e,*]

[a] *Department of Materials Science & Engineering, University of California, Berkeley, CA, 94720, USA*
[b] *Materials Science and Engineering Program, University of California San Diego, La Jolla, CA 92093, USA*
[c] *Department of Mechanical Engineering, University of California, Berkeley, CA, 94720, USA*
[d] *Department of Nanoengineering, University of California San Diego, La Jolla, CA 92093, USA*
[e] *Materials Sciences Division, Lawrence Berkeley National Laboratory, Berkeley, CA, 94720, USA*

ARTICLE INFO

ABSTRACT

Bouligand structures are widely observed in natural materials; elasmoid fish scales and the exoskeleton of arthropods, such as lobsters, crabs, mantis shrimp and insects, are prime examples. In fish scales, such as those of the *Arapaima gigas*, the tough inner core beneath the harder surface of the scale displays a Bouligand structure comprising a layered arrangement of collagen fibrils with an orthogonal or twisted staircase (or plywood) architecture. A much rarer variation of this structure, the double-twisted Bouligand structure, has been discovered in the primitive elasmoid scales of the coelacanth fish; this architecture is quite distinct from "modern" elasmoid fish scales yet provides extraordinary resistance to deformation and fracture. Here we examine the toughening mechanisms created by the double-twisted Bouligand structure in comparison to those generated by the more common single Bouligand structures. Specifically, we have developed an orientation-dependent, hyperelastic, phase-field fracture mechanics method to computationally examine the relative fracture toughness of elasmoid fish scales comprising single vs. double-twisted Bouligand structures of fibrils. The model demonstrates the critical role played by the extra inter-bundle fibrils found in coelacanth fish scales in enhancing the toughness of Bouligand-type structures. Synthesis and fracture tests of 3-D printed Bouligand-type materials are presented to support the modeling and complement our understanding of the fracture mechanisms in Bouligand-type structures.

© 2019 Elsevier Ltd. All rights reserved.

1. Introduction

The evolution of the integumentary skeletons of fish, in the form of their scales, reveals a pathway of how natural selection balanced and optimized their lightweight, flexibility and effective toughness to provide protection and retain mobility. Large juxtaposed plates in ancient fish could provide a protective shield but impeded movement and locomotion (Bruet et al., 2008; Wagner and Aspenberg, 2011). Boxfish, leatherback sea turtles and armadillos (Chen et al., 2011, 2015; Yang
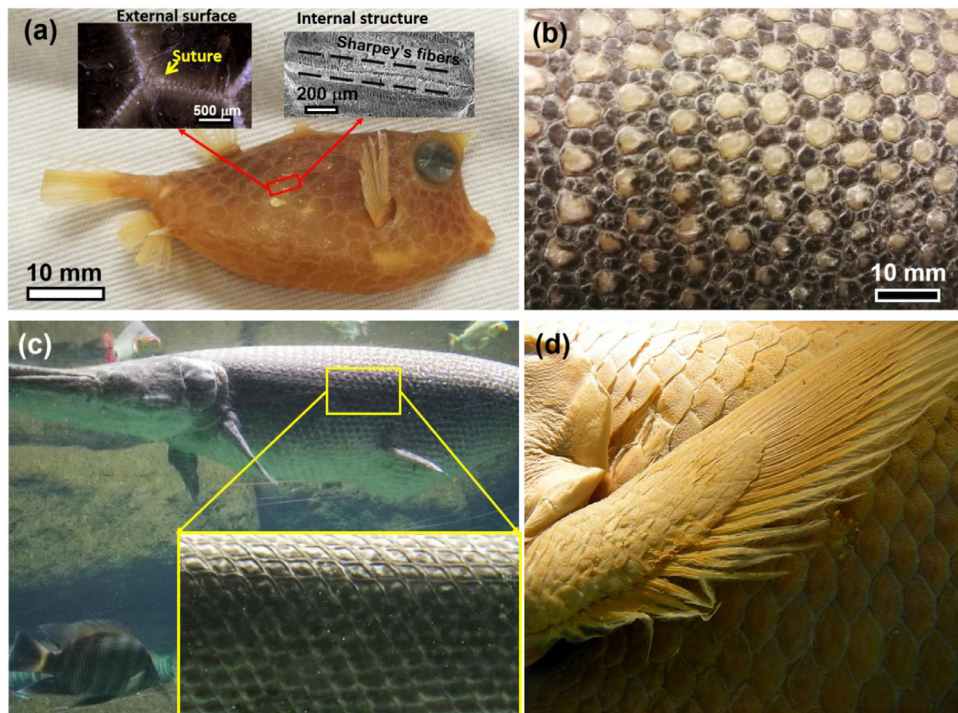

Fig. 1. Examples of biological connected units in natural scales. (a) Boxfish skin with juxtaposed scutes connected by the Sharpey's fibers (collagen fibers). (b) Armadillo osteoderm with juxtaposed plates connected by keratin. (c) *Alligator gar* overlapping (ganoid) scales with small degree of imbrication. (d) Coelacanth fish overlapping elasmoid scales with large degree of imbrication.

et al., 2015) still use this juxtaposed pattern to connect their structural features, as shown in Fig. 1a,b. During evolution, the juxtaposed fish plates separated and imbricated into smaller ones; a good example that still exists today is the *ganoid scale*, which possesses highly mineralized layers for penetration resistance (Yang et al., 2013b). However, such rigid individual units with a small degree of imbrication, *i.e.*, the ratio of their exposed length to total length, can severely compromise flexibility, as for example with the fish scales of the alligator gar shown in Fig. 1c. The prevailing type of fish scales today are *elasmoid scales* (Fig. 1d), which are much more compliant. They possess a hard outer layer to resist predatory attacks, but with a markedly reduced mineral content, and a tougher laminate inner core composed of non-mineralized or slightly mineralized collagen fibrils to accommodate the excessive deformation.

The tough inner core of many elasmoid scales, such as those of the carp and *Arapaima gigas* fish, exhibits a layered arrangement of collagen fibrils that follows an orthogonal or twisted staircase (or plywood) structure, known as the 'Bouligand-type' structure (Fig. 2a), where each layer is rotated with respect to the one directly adjacent to it. In this fashion, a helicoidal structure is produced that can be found in many different species. In the arapaima fish scale, the orientation of the collagen fibrils varies from layer to layer, which are designed to accommodate the imparted deformation and enhance the scale's toughness through fibrous collagenous lamellae rotation, fibril straining and interfibrillar sliding (Murcia et al., 2017; Quan et al., 2018; Torres et al., 2015; Yang et al., 2014; Zhu et al., 2012, 2013; Zimmermann et al., 2013); we term these *ductile* Bouligand structures. This architecture can also improve in-plane isotropy of structure since helically stacked highly aligned layers can better withstand omni-directional forces (Ling et al., 2018).

Bouligand structures are also widely observed in the exoskeleton of arthropods, such as lobsters (Al-Sawalmih et al., 2008; Raabe and Sachs, 2005; Sachs et al., 2006), crabs (Chen et al., 2008; Dennell, 1974), mantis shrimp (Guarín-Zapata et al., 2015; Suksangpanya et al., 2017; Tadayon et al., 2015) and insects (Yang et al., 2017a). These chitin-nanofibril-based natural materials are far stiffer and non-deformable compared to elasmoid fish scales (Dastjerdi and Barthelat, 2015; Quan et al., 2018; Yang et al., 2013a; Zimmermann et al., 2013). The Bouligand architecture in this type of material lead to a twisting crack front advance which serves to increase the fracture toughness primarily by crack deflection (Suksangpanya et al., 2017, 2018; Zaheri et al., 2018); we term these *brittle* Bouligand structures. Theoretical analyses of such twisted crack trajectories within these Bouligand structures have been proposed (Fischer et al., 2017; Suksangpanya et al., 2017) with the enhanced toughness attributed to the increment in crack-surface area and fracture mode-mixity. Recently, through the use of additive manufacturing techniques, fracture mechanisms have also been explored experimentally in fabricated biomimetic Bouligand-type materials (Chen et al., 2018; Feilden et al., 2017; Suksangpanya et al., 2018; Yang et al., 2017b; Zaheri et al., 2018). Computational approaches, such as finite element methods with a pre-defined cohesive interface, have also been applied to study the phenomenon of twisted cracks in the brittle form of the Bouligand structure (Suksangpanya et al., 2018).
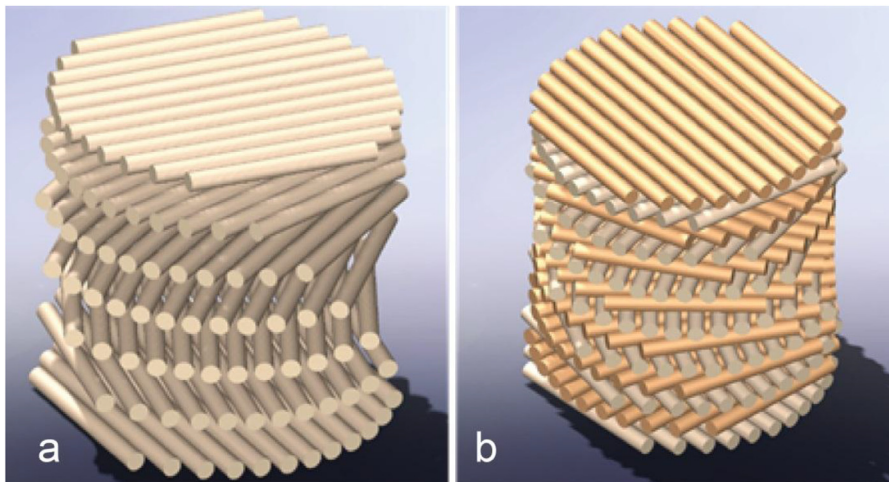
Fig. 2. Schematic illustrations of Bouligand structures. (a) Single Bouligand structure, typical of *Arapaima gigas* fish scales, and (b) the rarer double-twisted Bouligand structure, found in coelacanth fish (Quan et al., 2018). (Interbundle fibers in double-twisted Bouligand structure in coelacanth are not shown in these schematics).

There is a second type of Bouligand structure in nature, which is much rarer but has been found in the primitive type of elasmoid scales of Chordata fish (Giraud et al., 1978; Quan et al., 2018), such as the "living fossil" coelacanth fish and the Australian lung fish. This is the unique double-twisted Bouligand structure (Fig. 2b) that is quite distinct from the prevailing current elasmoid fish scales (Quan et al., 2018). Instead of being simply a twisted plywood structure, the double Bouligand structure uses the orthogonal bilayer as a unit to further form the twisted plywood structure, and has an array of fibrils perpendicular to the laminate structure, mainly along the thickness direction, called the interbundle fibrils; these hold the structure together and keep the bilayers from separating.

In this study, we use phase-field fracture mechanics methodologies to computationally examine the relative fracture toughness of the single vs. double-twisted Bouligand structures in laminated natural materials. Fracture tests of 3-D printed Bouligand-type materials further support the modeling and complement our understanding of the fracture mechanisms in Bouligand-type structures. We conclude that the toughest scale is achieved by the rare double-twisted Bouligand structure of lamellae, which is enhanced by the constraint provided by the extra inter-lamellae fibril bundles.

## 2. Characteristics of natural single and double-twisted Bouligand structures

Fig. 3 compares the single Bouligand structure of the carp fish scale and the double-twisted Bouligand of the coelacanth fish scale. The collagen fibrils of adjacent lamellae in the single Bouligand structure of carp fish scale show a ~60° rotation (Fig. 3a,b); however, in the coelacanth scale, the collagen fibrils form fiber bundles that orient to create an orthogonal bilayer, as shown in Fig. 3c,d (Quan et al., 2018). These bilayers act as units and rotate through the entire thickness of the coelacanth scale, forming the so-called double-twisted Bouligand structure. In addition, as noted above, the double-twisted Bouligand structure contains inter-bundle fibrils which constrain their rotation and shear and thereby decrease the damage of the structure.

Under tensile loading, fish scales with the ductile Bouligand structure are highly stretchable with multiple toughening mechanisms activated, including the rotation, stretching and delamination of the fibrillar lamellae. The lamellae separate readily when the scale is subjected to deformation, as shown in Fig. 4a (Yang et al., 2014). In contrast, fracture in the double-twisted Bouligand structure involves more complicated mechanisms, as can be seen at the tip of a loaded crack in the Coelacanth scale (Fig. 4b). Tri-dimensional effects due to the interbundle fibrils create a more complex crack-tip morphology. Indeed, Fig. 4c,d show the difference in the damage in the vicinity of a crack in the single vs. double-twisted Bouligand structure. Both show significant crack-tip broadening with resistance to crack propagation. In a larger arapaima fish scale in Fig. 4c, one can clearly see the orientation of the collagen fibers and how they become stretched at the blunted crack tip; a clear image of the more blunted crack in the coelacanth fish scales with double-twisted Bouligand structure, shown in Fig. 4d, indicates less delamination between the lamellae due to the constraint of the interbundle fibrils.

3. Computational modeling of fracture in the Bouligand-type structures

To explore the degree of toughening in natural materials and to compare two biological strategies, single vs. double-twisted Bouligand structures, we adopted an anisotropic phase-field fracture mechanics model. Due to the unique Bouligand architecture, the twisting nature of the crack front is essential to the modeling. Distinct from previous cohesive zone modeling, CZM, (Xu and Needleman, 1994) of the Bouligand structure, which required pre-defined crack interfaces
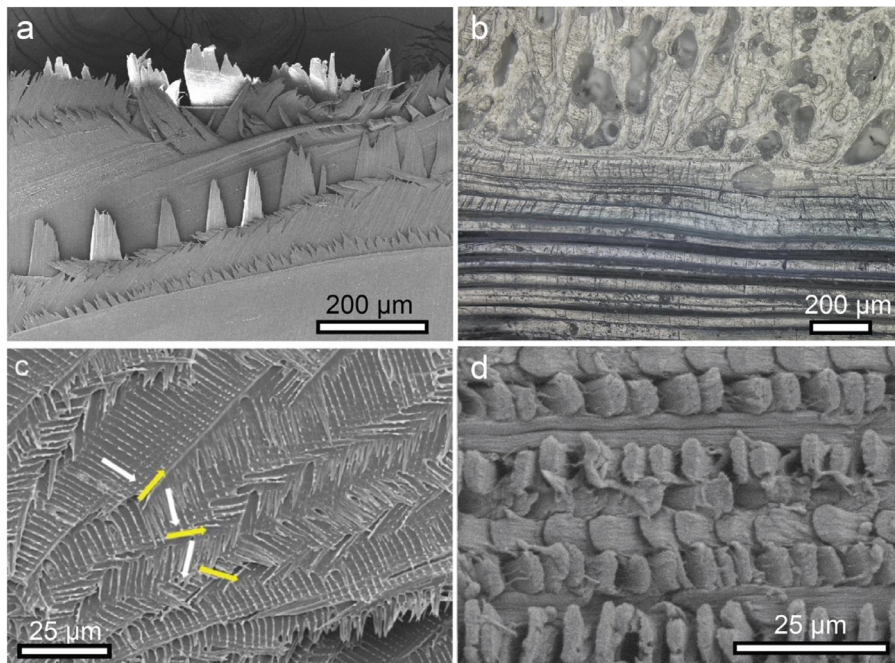
Fig. 3. Scanning electron microscopy images of single and double-twisted Bouligand structure. (a) Single Bouligand structure of carp scale, with (b) cross-sectional view. (c) Double-twisted Bouligand structure of coelacanth scale (Quan et al., 2018) with (d) cross-sectional view. Note significant difference in cross sectional organization between carp and coelacanth scales (b and d).
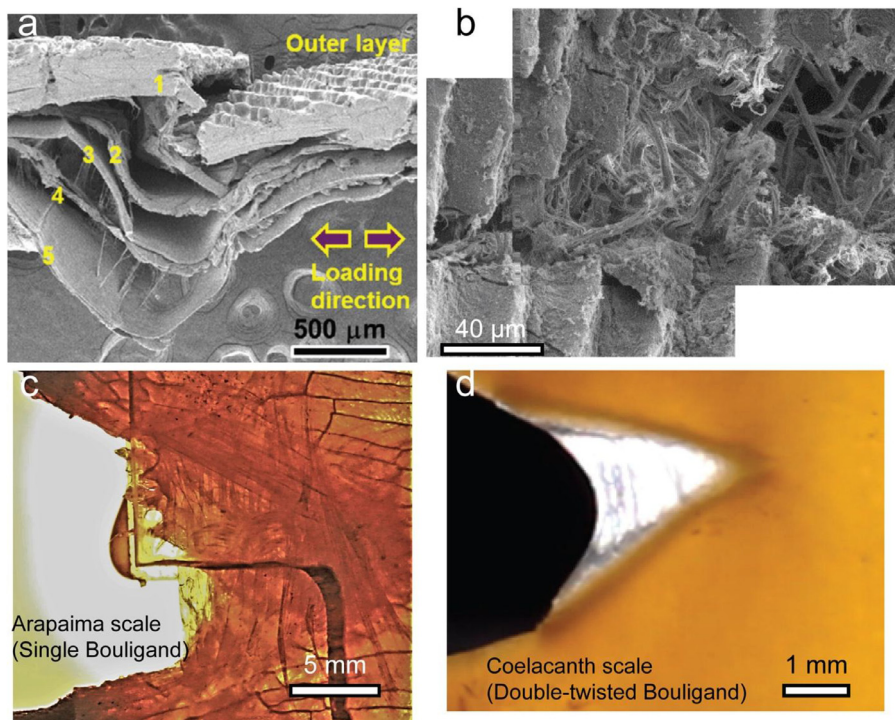
Fig. 4. Damage and crack tips in single and double-twisted Bouligand structures. (a) Surface damage of the arapaima fish scale with single Bouligand structure before fracture (Yang et al., 2014). (b) Corresponding damage in the vicinity of a crack tip in a double Bouligand structure under load (Quan et al., 2018). Experimental observation of tip of a tensile-loaded crack in (c) single and (d) double-twisted Bouligand structures.

(Suksangpanya et al., 2018), one key advantage of the phase-field fracture model lies in predicting complex crack paths which can capture the twisting front automatically.

The phase-field fracture method is based on the variational formulation of brittle fracture (Bourdin et al., 2000; Francfort and Marigo, 1998), and is mechanism-independent. By introducing the idea of a diffusive crack through a phase-field damage parameter (Bourdin et al., 2008; Miehe et al., 2015, 2010b), it can avoid the realization of sharp crack discontinuities and overcome the difficulty in capturing complex crack topologies. Recent extensions of the phase-field fracture method have been successfully applied to polymers (Miehe and Schänzel, 2014), polymeric gels (Mao and Anand, 2018; Mao et al., 2017), chemo-mechanical batteries (Miehe et al., 2016) and soft biological tissues (Gültekin et al., 2018; Raina and Miehe, 2016).

In biological tissues, the fracture behavior is anisotropic due to the highly oriented collagen fibrils in the stacked lamellae (Yang et al., 2017a). To account for this, an orientation-dependent phase-field fracture method has been developed with anisotropic surface energy depending on the underlying fiber direction (Gültekin et al., 2018; Li et al., 2015; Teichtmeister et al., 2017).

3.1. The anisotropic phase-field fracture model

In this work, we replace the strain-energy density function in the classical phase-field fracture model with a constitutive law more attuned to biological tissue, that of a hyperelastic law under a finite-strain framework, and adopt an anisotropic crack-surface density function (Teichtmeister et al., 2017) to model the deformation and fracture behavior of the individual lamellae in the Bouligand-type structures.

The pseudo-energy potential of the system can be written as:

$$\Gamma(\boldsymbol{u}, d) = \int_\Omega g(d)\Psi_e(u)d\Omega + \int_\Omega G_c\gamma_l(d, \nabla d)d\Omega, \tag{1}$$

where $\Omega \subset \mathbb{R}^3$ is the reference configuration of a material body in space, $d \in [0, 1]$ is the phase-field parameter, in which $d = 0$ represents undamaged material, and $d = 1$ represents totally damaged material. Ψ_e is the strain-energy density of the material, $\boldsymbol{u}$ is the displacement field, G_c is a parameter related to fracture energy, and $\gamma_l(d, \nabla d)$ is the crack-surface density function. A common degradation function $g(d) = (1 - d)^2 + k$ is adopted here, where k is small value for numerical stability.

The energy-based fracture criterion (Miehe et al., 2015) is used and the irreversibility of the damage evolution is achieved through a history-variable $H = \max_{s\in[0,t]} \Psi_e(\boldsymbol{u}, s)$. The problem can be split into two quasi-independent minimization procedures and a robust staggered scheme (Miehe et al., 2010a; Molnár and Gravouil, 2017) is implemented to solve the equations.

The anisotropic crack surface density function (Teichtmeister et al., 2017) is written as:

$$\gamma_l(d, \nabla d) = \frac{d^2}{2l_0} + \frac{l_0}{2}|\nabla d|^2 + \alpha(\nabla d \cdot \boldsymbol{a})^2, \tag{2}$$

where $\boldsymbol{a}$ is the material direction (fiber direction), l_0 is a length-scale parameter and α is an anisotropy coefficient.

The hyperelastic constitutive law is of the form:

$$\Psi_e = \frac{\mu}{\beta}\left(J^{-\beta} - 1\right) + \frac{\mu}{2}(tr(\boldsymbol{C}) - 3) + \frac{\chi}{4}(I_4 - 1)^2, \tag{3}$$

where $J = \det \boldsymbol{F}$, $\boldsymbol{F}$ is the deformation gradient, $\boldsymbol{C}$ is the right Cauchy-Green tensor, $I_4 = tr[\boldsymbol{CM}]$, $\boldsymbol{M} = \boldsymbol{a} \otimes \boldsymbol{a}$, μ is the shear modulus, and β and χ are material parameters. This form can be replaced by other constitutive laws for different material systems. Benchmark tests to verify this approach and representative numerical examples can be found in Appendix A. Further details of the nature of the phase-field fracture method can be found in literature (Miehe et al., 2010b; Molnár and Gravouil, 2017; Teichtmeister et al., 2017).

The basic unit of the Bouligand structure is a single lamella. To illustrate the anisotropic fracture in this basic unit, we consider a 3-D rectangular plate which contains a single-edge notch in the center. As shown in Fig. 5a, the bottom of the sample is fixed in vertical direction whereas a linearly increasing displacement u is applied at the top. The dimension of the single lamella is 5 mm x 10 mm x 0.05 mm and the length of initial crack is 2 mm. The anisotropic phase-field fracture model is implemented in this work using 8-noded isoparametric (3-D) elements. The material is as described above with fiber direction $\boldsymbol{a}$ which is inclined at an angle θ with respect to the horizontal direction. Other parameters used in the simulations are given in Table 1. In the literature (e.g., Sherman et al., 2015), the Young's modulus of collagen materials ranges from a few to several thousand MPa. Here we chose the Young's modulus to be $E = 100$ MPa with a Poisson's ratio of $\nu = 0.3$, which gave a shear modulus of $\mu = 38$ MPa with $\beta = \frac{2\nu}{1-2\nu} = 1.5$. The energy stored in collagen fiber configurations is taken as the anisotropic portion of the energy, as has been extensively proposed in the literature (Itskov and Aksel, 2004; Schröder and Neff, 2003; Schröder et al., 2008). Here we adopted a simplified form: $\frac{\chi}{4}(I_4 - 1)^2$, with χ chosen as 0.2% of the shear modulus. G_c is the characteristic critical energy release rate, which is set as 1 N·mm^{-1}. l_0 is the characteristic length-scale that determines the width of the diffusive crack; according to the results of Miehe et al. (2010b), this length-scale parameter is always taken to be two times larger than the smallest element around the crack path. α is the anisotropy coefficient. For higher α values, the anisotropic effect is stronger and crack is more likely to propagate along the fiber direction. The α term also contributes to the value of characteristic fracture energy. In current model, we chose $\alpha = 10$ since this value can guarantee the deflection of crack along fiber direction, as shown in Fig. 5. Varying these material parameters will change
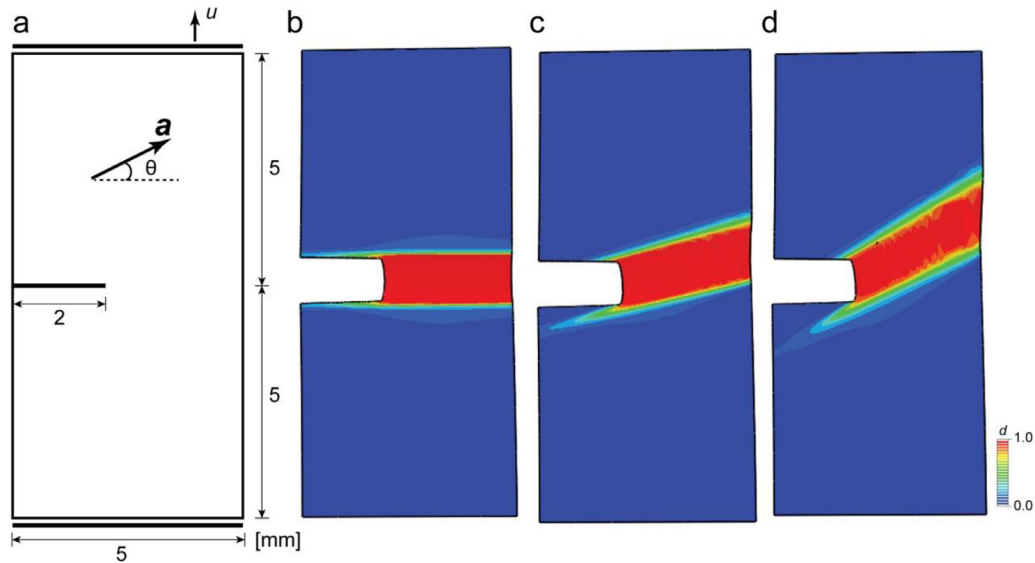
Fig. 5. Anisotropic phase field fracture. (a) Single-edge notched plate under uniaxial tensile loading. a is the fiber direction and θ is the fiber direction angle. Fractured sample with a fiber direction angle of (b) $\theta = 0°$, (c) $\theta = 15°$, and (d) $\theta = 30°$. False colors shown with blue representing the undamaged material and red the damaged material.

Table 1
Material properties used in anisotropic phase field fracture model.

| Parameter	Dimension	Material Property	Value
l_0	mm	characteristic length-scale	0.05
α	–	anisotropy coefficient	10
G_c	N·mm^{-1}	characteristic fracture energy	1
μ	MPa	shear modulus	38
β	–	constitutive coefficient	1.5
χ	MPa	constitutive coefficient	0.077

the absolute value of toughness that is predicted by the model, but the fracture mechanisms, especially differences in the crack-tip morphology, and the relative toughness between the single and double-twisted Bouligand structures will remain unchanged. Fig. 5b–d show the propagation of the fracture for different fiber direction angles ranging from $\theta = 0°$, 15° and 30°. The anisotropic fracture is captured such that the crack follows the fiber direction a under the current settings.

With this basic unit of a single lamella, we can investigate the effect on the fracture properties of single and double-twisted Bouligand structures by setting up a 3-D multi-layer finite element model in which each layer possesses a specific fiber orientation a, as depicted in Fig. 6a. Multiple layers stacked together with a specific twist angle arrangement can represent the single or double-twisted Bouligand structure. Between the lamellae, we can specify different constraints, i.e., with no interaction, with perfect bonding, or represented by a set of nonlinear springs, depending upon the specific nature of the natural structures. These constraints represent the differing strength of interactions between the individual layers, and will be shown to play an important role in the fracture toughness of the resulting structure, as further described below.

3.2. Simulation results

The current model contains 12 different layers with different fiber orientations, in which the angle of twist θ ranges from $-90°$ to 75° with an equal difference. For the single Bouligand structure, the stacking angles are arranged as: $-90°$, $-75°$, $-60°$, $-45°$, $-30°$, $-15°$, $0°$, $15°$, $30°$, $45°$, $60°$, $75°$, while the stacking angles for double-twisted Bouligand structure are: $0°$, $-90°$, $15°$, $-75°$, $30°$, $-60°$, $45°$, $-45°$, $60°$, $-30°$, $75°$, $-15°$. These represent typical stacking sequences in fish scales, respectively for the *Arapaima gigas* (Yang et al., 2014) and coelacanth (Quan et al., 2018). Periodic boundary conditions (Wu et al., 2014) are applied in the stacking direction. An identical loading condition to that in Fig. 5a is applied to the multi-layer model.

Fig. 6b shows the simulated stress–strain curves for the single and double-twisted Bouligand structures with either perfect bonding (blue and red curves) or no interaction conditions between the layers (black curve). For the latter case of no interaction between the differently oriented layers, which we define as the "independent layers" case, the total stress–strain curve is simply the average of the stress–strain curves from all of the different individual lamella; the specific architecture
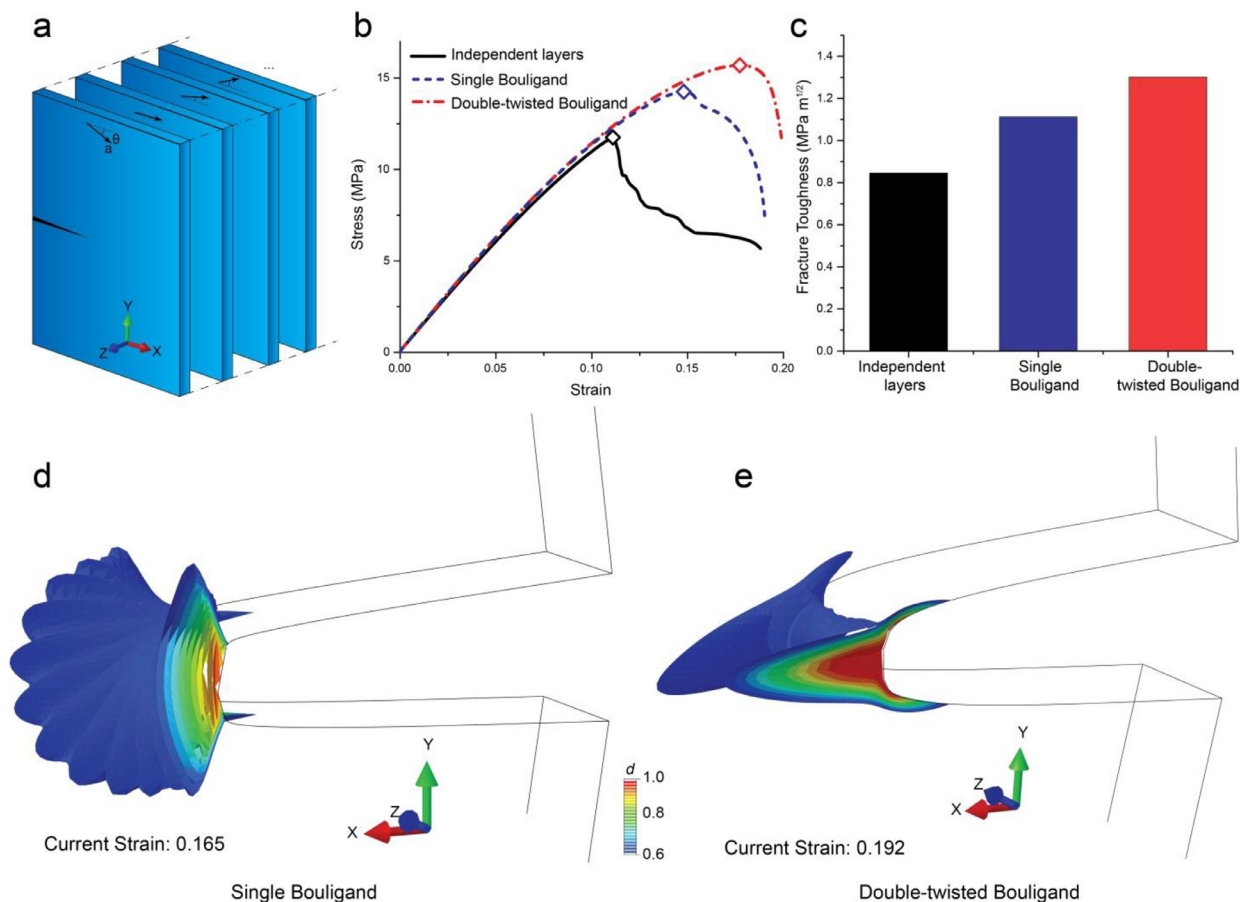
Fig. 6. Simulation results of fracture in Bouligand-type materials. (a) 3-D multi-layer finite element model in which each layer possesses a specific fiber orientation *a*. (b) Stress–strain curves of single and double-twisted Bouligand structures with either perfect bonding or no interaction conditions between the layers (diamond markers represent the peak stress on each curve). (c) Estimated fracture toughness values. Morphology of crack-tip damage in (d) the single Bouligand structure and (e) the double-twisted Bouligand structure. False colors represent phase-field parameter *d* in a range from 0.6 to 1 (*d* defines the degree of damage; $d = 0$ represents undamaged material, $d = 1$ represents fractured material).

of the single or double-twisted Bouligand has no effect during deformation and the stress–strain curves converge to the black curve in Fig. 6b. Due to the highly anisotropic properties of the different layers, the initiation of the crack is different between the layers. Apparently, the lamella with a fiber orientation perpendicular to the tensile direction will sustain more mode-I loading and the crack will initiate and propagate firstly in those layers. Multiple stress drops were observed in the black (independent layers) curve; these drops represent the initiation of cracking in the different layers.

For the case of perfect bonding between the layers, *i.e.*, computationally achieved by sharing nodes between layers, the red curve in Fig. 6b corresponds to the stress–strain curve for the double-twisted Bouligand structure and the blue curve to the single Bouligand structure. By integrating the area under stress–strain curves up to the maximum stress (Shin et al., 2016), where the critical energy release rate is given by $G = 2Hb \int_0^{\epsilon_0} \sigma \, d\epsilon$, where H is the half width of the strip, b is the thickness, and ϵ_0 is the critical strain at the peak stress, and converting to a stress-intensity factor, we can estimate the relative fracture toughness of the two structures and compare this with the toughness for the independent layer case. As shown in Fig. 6c, the fracture toughness of the single and double-twist Bouligand structures are both higher, respectively by 32% and 54% for the perfect bonding condition, compared with the independent case. Specifically, the double-twisted Bouligand structure is predicted to be roughly 17% tougher than the single Bouligand structure.

These stress–strain curves indicate that the double-twisted Bouligand structure can sustain a higher magnitude of loading before crack initiation, with a roughly 20% higher critical strain for fracture than the single Bouligand structure. Examination of the fracture process during the simulation reveals significant differences in the morphology of crack-tip front between the single and double-twisted Bouligand structures. As shown in Fig. 6d,e, in the single Bouligand structure, a continuous, twisted crack tip is formed on loading, with a relatively sharp damage zone developed ahead of it. In contrast, the double-twisted Bouligand structure has a blunter and straighter crack tip; damage development is first observed in layers where the fiber orientation is perpendicular to the loading direction, *i.e.*, which sustains more mode-I loading, such that the overall
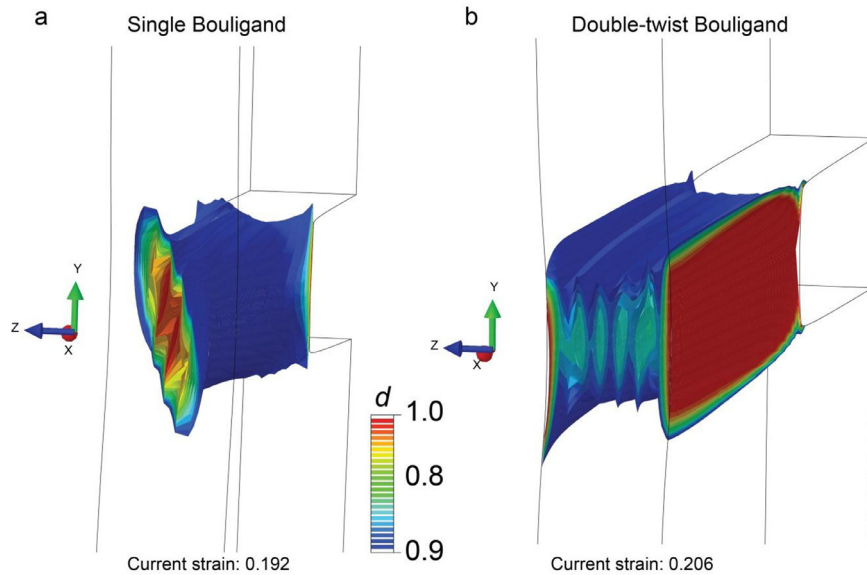
Fig. 7. Simulated morphologies of crack-tip damage in their final state. Morphologies of crack-tip damage in (a) the single Bouligand structure and (b) the double-twisted Bouligand structure. False colors represent phase-field (damage) parameter d in a range from 0.9 to 1. There is a clear twist in the fracture surface in the single Bouligand structure, which is not apparent for the double Bouligand structure.

crack patch is constrained in this direction and the complete crack front between the layers is far more blunted than that for the single Bouligand structure. Videos of such simulated 3-D morphologies of the damage field at the crack tip for the single and double Bouligand structures are available in the Supplementary Materials. Fig. 7 shows these morphologies of crack-tip damage in their final states. Consistent with the initial crack damage fields shown in Fig. 6e, there is a clear twist on the fracture surface in the single Bouligand sample, shown in Fig. 7a, whereas in the double-twisted Bouligand sample, the fracture surface is more blunted and straighter (Fig. 7b).

The crack-tip damage zones predicted by the current phase field model (Figs. 6e,d, 7) are consistent with the crack-tip morphology in 3-D printed synthetic Bouligand samples discussed below. Moreover, up to the onset of catastrophic failure, significantly more energy can be dissipated through the creation of multi-layer damage in the double-twisted structure, as the damage zone, defined by the volume of elements with $d > 0.95$ in the undeformed configuration (Fig. 7), in the double-twisted Bouligand structure is significantly (∼60%) larger than that in the single Bouligand structure.

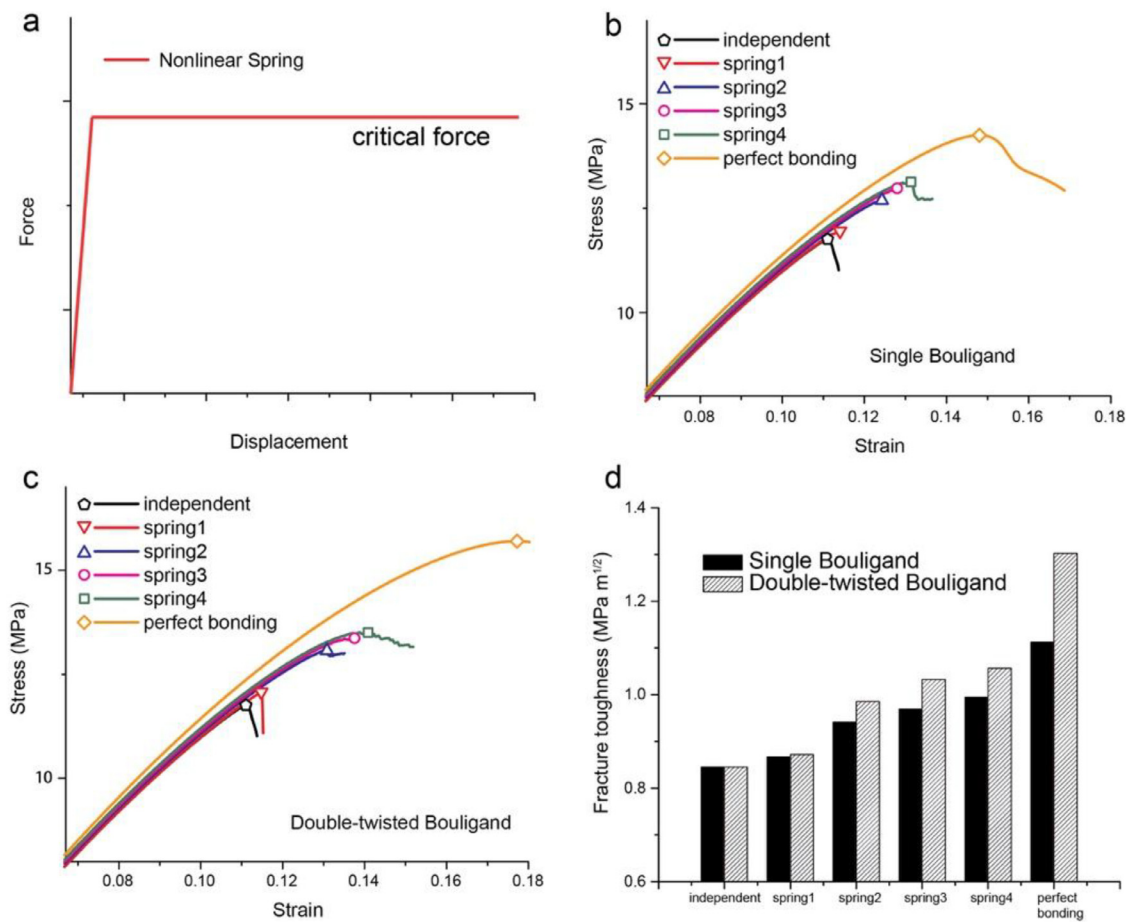### 3.3. Role of interfibrillar shear strength

Based on the above predictions of the fracture toughness of the Bouligand structures with either perfect interlayer bonding or with no bonding, *i.e.*, for the case of independent layers, it is evident that the interfibrillar shear strength between different lamellae plays a key role in the resulting toughness of the Bouligand architecture.

If there is no bonding between the layers (independent layer case), the Bouligand twisted plywood structure cannot contribute to the total toughness of the material and the effect of all the different stacking sequences will vanish and the structure will converge to the same constitutive behavior, designated by the black line in the stress–strain curve in Fig. 6b. Perfect bonding here means the neighboring lamellae in the finite-element mesh share the same nodes on the contact surfaces, which is an ideal situation where the interfibrillar shear strength is infinite. The case of perfect bonding thus provides an upper limit of the confinement from neighboring lamella to the fracture opening and represents the situation where the toughening generated by the Bouligand structure is maximized.

In actual natural materials, clearly the interfibrillar shear strength is finite (Szczesny and Elliott, 2014) and determined by the organic matrix, mineralization of the fibrils and reinforcement by extra fibril bundles. To model the specific effect of the interfibrillar shear strength for the toughening mechanisms generated by actual Bouligand structures, we connect coincident pairs of nodes on neighboring lamellae by nonlinear springs with a tunable strength in the simulations. The force-displacement curve of the nonlinear spring is shown in Fig. 8a. We have taken the spring constant here to be $100\,\mathrm{N{\cdot}mm^{-1}}$; once a critical force is reached, it maintains a constant force with further stretching. The interfibrillar shear strength is thus tunable by this critical force and can be calculated through the density of the springs on the contact plane. The critical forces and interfibrillar shear strengths of four different springs used in our simulations are provided in Table 2.

By tuning the critical force of the nonlinear springs, interfibrillar shear strengths can be changed, as shown in Table 2, which can have a marked effect on the magnitude of the toughening induced by the Bouligand structure. Fig. 8b,c, respectively, show the stress–strain curves of the single and double-twisted Bouligand structures with different interfibrillar

Fig. 8. Role of interfibrillar shear strength. (a) Schematic force-displacement curve of a nonlinear spring. (b) Stress–strain curves of the single Bouligand structure. (c) Stress–strain curves of the double-twisted Bouligand structure (hollow symbols represent the peak stress on each curve). (d) Fracture toughness of Bouligand structures as a function of the interfibrillar shear strength.

Table 2
Critical forces and interfibrillar shear strengths of nonlinear springs.

| Nonlinear Spring	Critical Force (N)	Interfibrillar shear strength (MPa)
1	1×10^{-4}	0.25
2	1×10^{-3}	2.5
3	2×10^{-3}	5
4	5×10^{-3}	12.5

shear strengths. The peak strength can be seen to progressively increase from the independent layer case (zero interfibrillar shear strength) to the perfect bonding case. The fracture toughness values for all these cases are shown in Fig. 8d, where the striped columns represent the double-twisted Bouligand structure and the black columns the single Bouligand structure. The simulations reveal that the fracture toughness of both Bouligand structures increases monotonically with the interfibrillar shear strength. This implies that if the interfibrillar shear strength is minimal, the single and double-twisted Bouligand structures have the same toughness. However, as the interfibrillar shear strength become stronger, the double-twisted Bouligand configuration becomes the tougher structure with the difference progressively increasing with higher interfibrillar shear strength, highlighting the critical role of the interfibrillar shear strength in the fracture of Bouligand-type structures.

4. Interbundle fibers in double-twisted Bouligand scale

For the coelacanth fish scale, extra interbundle fibers were found along with the double-twisted Bouligand structure (Quan et al., 2018). Fig. 9 shows a scanning electron microscopy (SEM) image of the cross-section of a coelacanth scale, in which the white arrows indicate the cross-sections of collagen fiber bundles in one lamella. There are extra interbundle
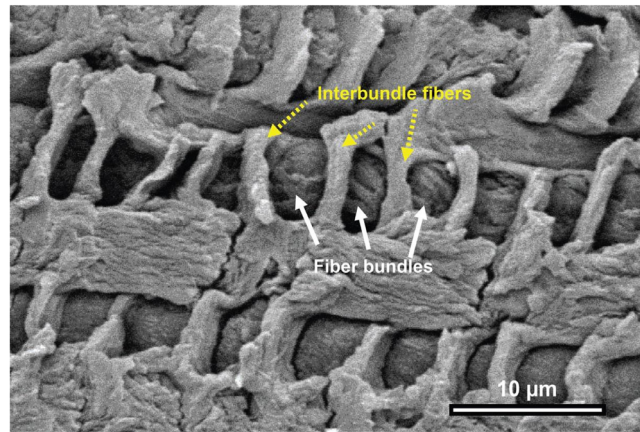
Fig. 9. SEM image of interbundle fibers in the double-twisted Bouligand coelacanth fish scale. Yellow dashed arrows show the interbundle fibers in the scale; white arrows indicate the collagen fiber bundles within the layer. (For interpretation of the references to color in this figure legend, the reader is referred to the web version of this article.)
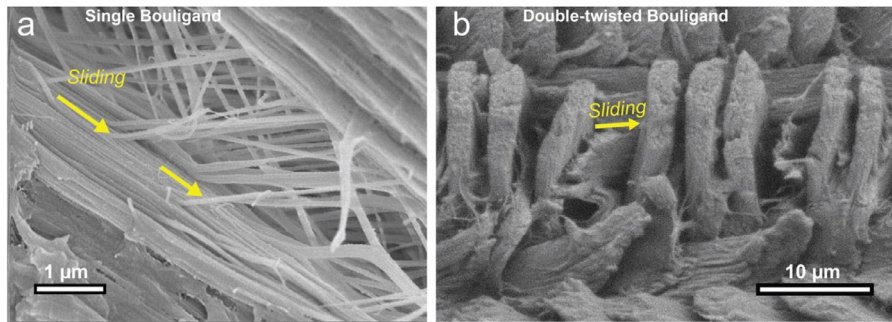

Fig. 10. SEM images of collagen fibrils sliding in the (a) single and (b) double-twisted Bouligand structures: for (a) single Bouligand structure of the arapaima scale, and (b) double Bouligand structure of the coelacanth scale.

fibrils between each collagen fiber bundle, as indicated by the yellow dashed arrows in Fig. 9. These unique interbundle fibrils, which are not observed in the single Bouligand structure, *e.g.*, in the arapaima fish scale, can play a critical role in enhancing the interfibrillar shear strength and hence the toughness of the double-twisted Bouligand structure.

Interfibrillar sliding in collagenous systems is a prime plastic deformation mechanism and hence contributes to the toughening of fish scales. Based on *in situ* small-angle x-ray scattering measurements on such scales under load, this mechanism has been shown to contribute to the global strain of the entire Bouligand structure, as compared to the smaller local strain within the collagen fibrils (Quan et al., 2018; Yang et al., 2014; Zimmermann et al., 2013), consistent with our model predictions that interfibrillar shear strength plays a critical role in establishing the fracture toughness of Bouligand-type structures. Specifically, the existence of interbundle fibers serves to substantially increase interfibrillar shear strength, and this is one of the prime reasons for the increased fracture toughness of the double-twisted Bouligand materials. Fig. 10a shows the sliding, peeling and delaminating of collagen fibrils in the single Bouligand structure under the tensile loading. However, in contrast, in the double Bouligand structure with interbundle fibers, such sliding first occurs between the interbundle fibers and collagen fibrils, and then within the collagen fibrils themselves, as shown in Fig. 10b where sliding of the collagen fibrils between the interbundle fibers, along with the rotation of the fibers, takes place under tensile loading. Although the existence of such interbundle fibers may enlarge the thickness of the collagen lamellae in the coelacanth fish scale, which serves to lessen its flexibility and locomotion, it can substantially enhance the fracture toughness through its concomitant enhancement in the interfibrillar sliding stress.

5. Synthesis and testing of Bouligand-type materials through 3-D printing

To complement our understanding of the evolution of damage and toughening mechanisms during fracture in single and double-twisted Bouligand structures and to verify the modeling predictions, we employed 3-D printing to fabricate synthetic Bouligand materials which were fractured during tension tests. This follows the methodology proposed by Velasco et al. (Velasco-Hogan et al., 2018) which consists of using 3-D printing to generate bioinspired constructs to assist in the understanding of structural principles. Similar to the geometry used in the computational modeling, the samples were fabricated in a rectangular plate shape with a single-edge notch, in a lamellar structure made from a soft polymeric material
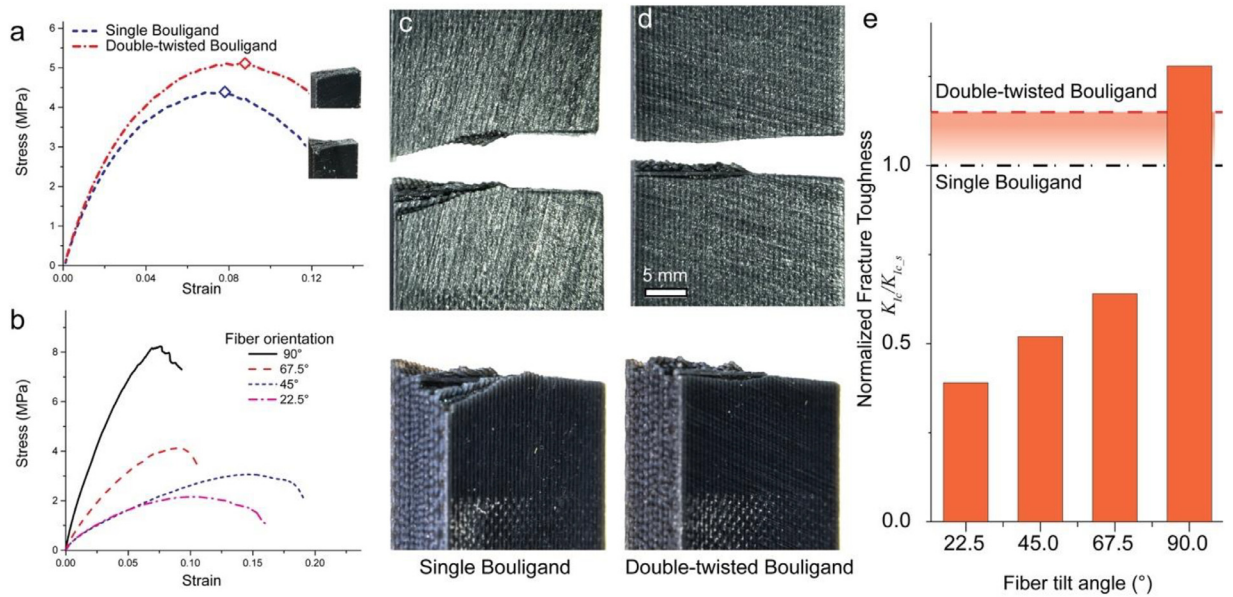
Fig. 11. Mechanical testing of synthetic Bouligand and non-Bouligand samples. (a) Stress vs. strain curves for the 3-D printed single and double-twisted Bouligand samples. The inserts show the fracture surface of each sample. (b) Stress vs. strain curves of 3-D printed non-Bouligand samples with single fiber orientation. (c) Cracked single Bouligand sample. (d) Cracked double-twisted Bouligand sample. (e) Normalized toughness of the non-Bouligand structured samples as a function of fiber tilt angle, in comparison to that of the single and double Bouligand structures; synergy is clearly demonstrated.

containing hard cylinders to simulate the fibers. Each sample contains 12 layers with different fiber orientations. The stacking angles in single and double-twisted Bouligand samples were the same as in computational model in Section 3.2. Details of the fabrication and mechanical testing of synthetic Bouligand samples are provided in the Appendix B.

Fig. 11a shows the stress–strain curves of the fabricated Bouligand structures. Consistent with the phase-field modeling, the double-twisted Bouligand structure can sustain 16% higher magnitude of loading before crack initiation. The fracture toughness is obtained by integrating the load-displacement curves up to the maximum load point and then converting to a stress-intensity factor; the toughness of double-twisted Bouligand structure is 15% higher than that of the single Bouligand structure, which is very close to the 17% value predicted by the modeling. The inserts in Fig. 11a show the fracture surfaces of the two different synthetic Bouligand structures. The fractured single Bouligand sample, shown in Fig. 11c, clearly displays a continuous twisted crack surface, whereas, in contrast, the crack path in the double-twisted Bouligand sample is far straighter with no twisting observed on the crack surface (Fig. 11d). Such crack-tip damage and subsequent crack-path trajectories in the synthetic Bouligand materials compare well with the corresponding predicted morphologies from the phase-field modeling (Fig. 7a,b).

As a reference, we also 3-D printed synthetic samples with only one fiber direction. Again, following the definition of fiber angle in Fig. 6a, these non-Bouligand structures contained single fiber orientations at angles of 90°, 67.5°, 45° and 22.5°. As expected, the non-Bouligand samples show highly anisotropic elastic and fracture properties which depend on the relative orientations between fibers, initial crack length and loading, as shown by the experimentally measured stress–strain curves in Fig. 11b. The 90° sample, where the fibers align along the loading direction, i.e., perpendicular the initial crack, can sustain most loading; here the sample fails by fracture of the fibers and generates the highest toughness. When the fibers are oriented at an angle to the loading direction, the sample becomes weaker as the crack is able to deflect and propagate into the soft matrix along the fiber directions. In Fig. 11e, the fracture toughness of all synthetic Bouligand and non-Bouligand samples are plotted and normalized by the toughness of single Bouligand sample K_{Ic_s}. It is apparent that only the 90° non-Bouligand sample (with fibers aligned along the loading direction) is tougher than the Bouligand samples; all the other single-fiber orientation structures are significantly less tough than the Bouligand samples, both single- and double-twisted. These results clearly demonstrate the synergistic effect of the Bouligand structures in improving the isotropy and toughness properties of natural lamellar structures.

6. Conclusions

In summary, we have used anisotropic phase-field fracture mechanics methodologies incorporating hyperelastic constitutive laws to computationally examine the relative fracture toughness of the single vs. double-twisted Bouligand structures, commonly seen in biological materials such as fish scales and the exoskeletons of arthropods, to reveal the underlying differences in the salient toughening mechanisms developed by the two natural architectures. We conclude that the highest toughness is achieved in the rarer double-twisted Bouligand structure of lamellae, as found in the elasmoid scales of the
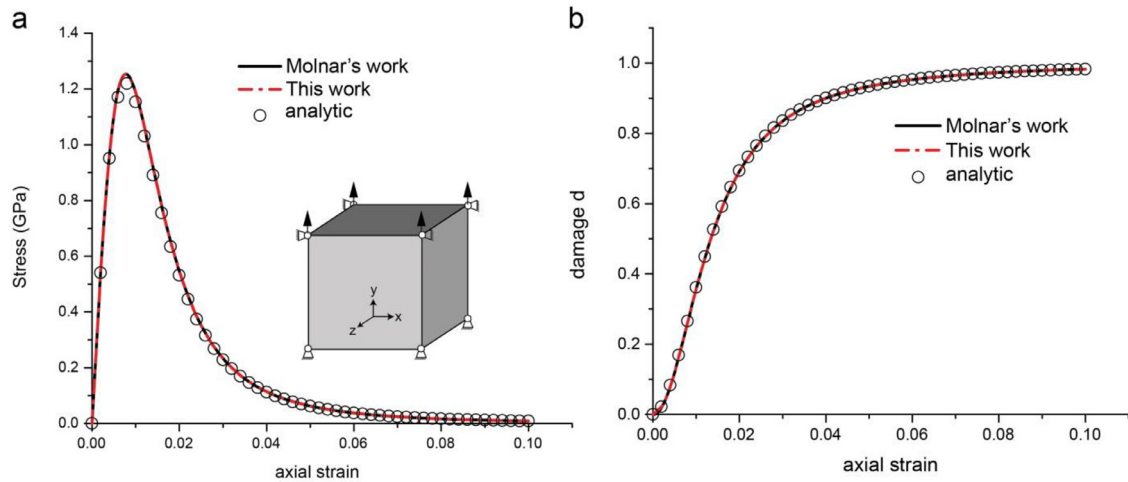
Fig. A1. One element test (linear elastic version). (a) Axial stress as a function of axial strain for the one element in uniaxial tension. The insert shows the element and boundary conditions. (b) Damage parameter d as a function of applied axial strain. The black line represents the results from Molnár's code, the red dashed line represents the results of this work and black circles represent the analytic solutions. (For interpretation of the references to color in this figure legend, the reader is referred to the web version of this article.)

coelacanth fish; our modeling thus highlights the critical role of inter-lamellae fibril bundles which act to increase the toughness of the material at the expense of its flexibility. Our modeling results were found to be consistent with experimentally measured mechanical properties of synthetic, 3-D printed, polymeric Bouligand materials, where uniaxial tensile tests on single-edge notched tension specimens confirmed the higher toughness of the double-twisted Bouligand structure and the difference in the crack-tip damage and fracture-surface morphology of the single vs. double-twisted structures. Additional comparisons between these Bouligand structures and 3-D printed non-Bouligand structures with only a single fiber orientation (which were naturally highly anisotropic) reveal the advantages of Bouligand structures in promoting the isotropy and enhanced fracture toughness properties of Nature's lamellar structures.

Competing interests

The authors declare no competing interests, financial or otherwise.

Acknowledgements

Appendix A. Benchmark tests and representative numerical examples

We demonstrate the veracity of the implemented phase field fracture mechanics model in this work by comparing with previous models, analytic solutions and a representative numerical example.

Our phase field fracture model was implemented through the AceGen platform (Korelc, 2002), in which the strain energy constitutive law Ψ_e and crack-surface density function $\gamma_l(d, \nabla d)$ can be conveniently altered and generate user elements automatically.

A1. One element test (linear-elastic version)

To verify our implementation of the model with the AceGen platform, we first generate a linear-elastic version of phase field fracture model and compare the one element test results with analytical solutions and the code provided by Molnár and Gravouil (2017).

The strain energy function used here is the linear-elastic function: $\Psi_e = \frac{\lambda}{2} \, tr(\epsilon)^2 + \mu \, tr(\epsilon.\epsilon)$ with the crack-surface density function the same as in Eq. (2). A 3-D 8-node element with $1 \times 1 \times 1$ mm dimension is used here. The bottom nodes of the element are constrained in all directions and the top nodes are allowed to slide in y direction, as shown in Fig. A1a. All the parameters are set to be the same as benchmarks in Molnár and Miehe's work (Miehe et al., 2010b; Molnár and Gravouil, 2017). The Young's modulus of the element is set to $E = 210$ kN/mm^2 and the Poisson's ratio to $\nu = 0.3$. The
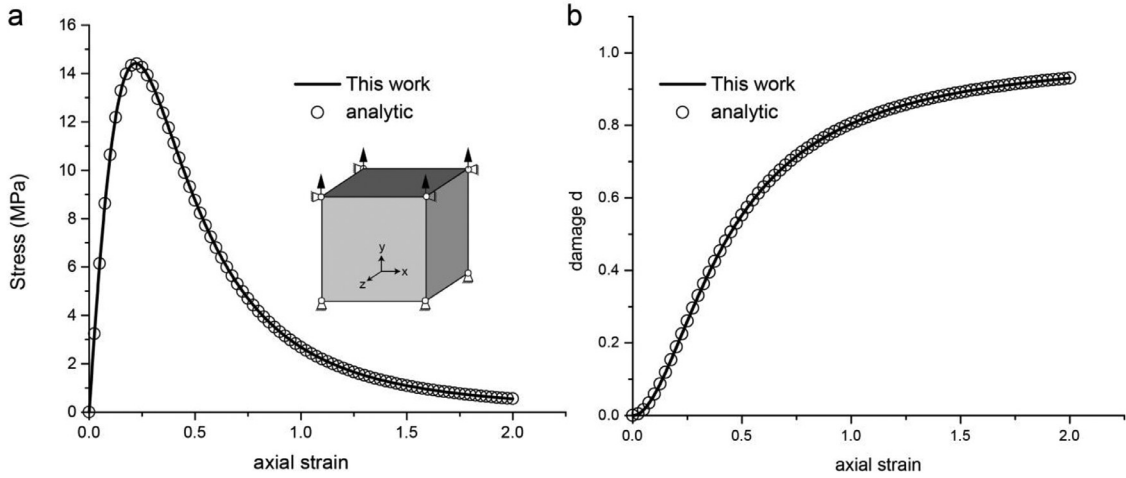
Fig. A2. One element test (finite strain, hyperelastic version). (a) Axial stress as a function of axial strain for the one element in uniaxial tension. The insert shows the element and boundary conditions. (b) Damage parameter d as a function of applied axial strain. The black line represents the results of this work; the black circles represent the analytical solutions.

critical energy release rate is $G_c = 0.005$ kN/mm and the length-scale parameter is $l_0 = 0.1$ mm. The anisotropic parameter α is set to be 0.

The uniaxial tension of one element can be solved analytically. According to the boundary condition, we have $u_y \neq 0$, $u_x = u_z = 0$; accordingly, the elastic energy is $\Psi_e = \frac{\lambda}{2}\,\epsilon_y^2 + \mu\,\epsilon_y^2 = \frac{E(1-\nu)}{2(1+\nu)(1-2\nu)}\,\epsilon_y^2$. The phase parameter can then be solved by minimizing Eq. (A1), *viz*:

$$\Gamma(d) = \int_{\Omega} g(d)H d\Omega + \int_{\Omega} G_c \gamma_l(d, \nabla d) d\Omega = \int_{\Omega}\left[G_c\frac{d^2}{2l_0} + (1-d)^2 H\right]d\Omega, \tag{A1}$$

in which $\nabla d = 0$ for this test.

Thus, the analytical solution of phase parameter is given by:

$$d = \frac{2H}{\frac{G_c}{l_0} + 2H} = \frac{2\Psi_e}{\frac{G_c}{l_0} + 2\Psi_e} = \frac{\frac{E(1-\nu)}{(1+\nu)(1-2\nu)}\epsilon_y^2}{\frac{G_c}{l_0} + \frac{E(1-\nu)}{(1+\nu)(1-2\nu)}\epsilon_y^2}. \tag{A2}$$

The corresponding axial stress can be written as: $\sigma_y = \frac{\partial \Psi_e}{\partial \epsilon_y} = \frac{E(1-\nu)}{(1+\nu)(1-2\nu)}\epsilon_y$, such that the degradation function can be described as:

$$\tilde{\sigma}_y = \frac{E(1-\nu)}{(1+\nu)(1-2\nu)}\epsilon_y * \left[(1-d)^2 + k\right]. \tag{A3}$$

Fig. A1a shows the axial stress computed using the Molnár's code, together with the analytical solution (Eq. (A3)). Fig. A1b shows the phase-field parameter d as a function of the applied strain. Fig. A1a,b demonstrate that using the current implementation of the phase-field fracture model, we can obtain exactly the same solution as the Molnar's code and agree closely with the analytical solution (Eqs. (A2–A3)).

A2. One element test (finite strain, hyperelastic version)

To verify our implementation of the model with a hyperelastic constitutive law in finite strain, the implemented user-defined element used here is created by replacing the strain energy function as $\Psi_e = \frac{\mu}{\beta}(J^{-\beta} - 1) + \frac{\mu}{2}(tr(\mathbf{C}) - 3) + \frac{\chi}{4}(I_4 - 1)^2$ in our AceGen platform while the crack-surface density function remains unchanged, as Eq. (2). A 3-D 8-node element with $1 \times 1 \times 1$ mm dimensions is used here. The bottom nodes of the element are constrained in all directions and the top nodes are allowed to slide in y direction, as shown in Fig. A2a. In this case, all the parameters are set to the same values as used in the manuscript. The Young's modulus of the element is set to $E = 100\text{N/mm}^2$ and the Poisson's ratio to $\nu = 0.3$. $\chi = 0.077\text{MPa}$. The critical energy release rate is $G_c = 1\text{N/mm}$ and the length-scale parameter is $l_0 = 0.05\text{mm}$. The anisotropic parameter α is set to be 0 and the fiber direction $\boldsymbol{a} = (1, 0, 0)$.
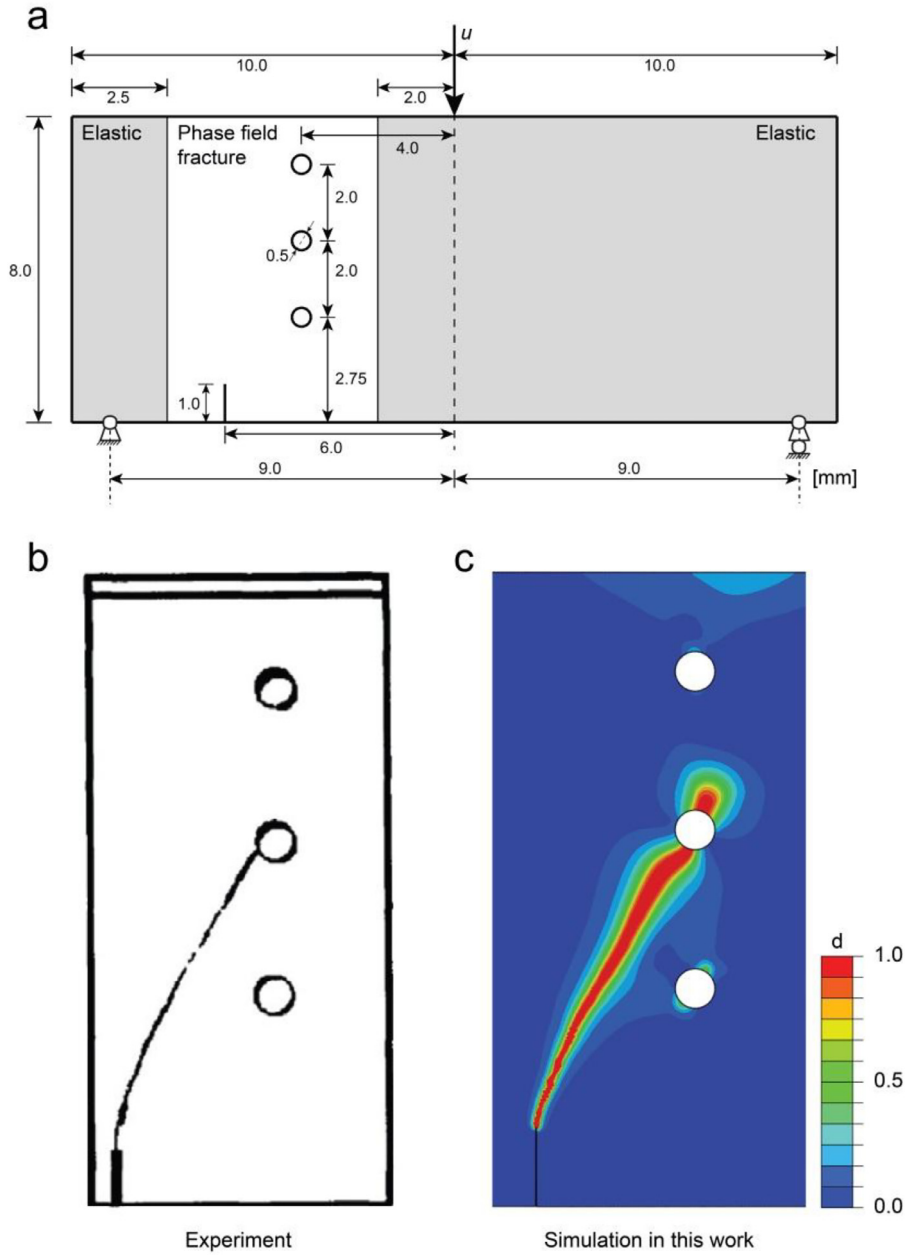
Fig. A3. Perforated asymmetric bending test. (a) Geometry and boundary condition for the perforated asymmetric bending sample. All the holes are 0.5 mm in diameter. To prevent local damage at loading and pinning points in the simulation, these regions remain elastic region such that d is kept as 0. (b) Fracture pattern observed in the experiments of Bittencourt et al. (1996), as compared with (c) the fracture pattern predicted in the current simulation.

Similarly, the uniaxial tension of one element can be solved analytically. According to the boundary condition, we have $u_y \neq 0$, $u_x = u_z = 0$, thus the deformation gradient is given by:

$$\boldsymbol{F} = \begin{bmatrix} 1 & 0 & 0 \\ 0 & 1 + \epsilon_y & 0 \\ 0 & 0 & 1 \end{bmatrix}. \tag{A4}$$

Accordingly, we can obtain $J = det\boldsymbol{F} = 1 + \epsilon_y$, $tr(\boldsymbol{C}) = (1 + \epsilon_y)^2 + 2$ and $I_4 = 1$. Thus, the strain energy as a function of axial strain ϵ_y is: $\Psi_e = \frac{\mu}{\beta}((1 + \epsilon_y)^{-\beta} - 1) + \frac{\mu}{2}((1 + \epsilon_y)^2 - 1)$.
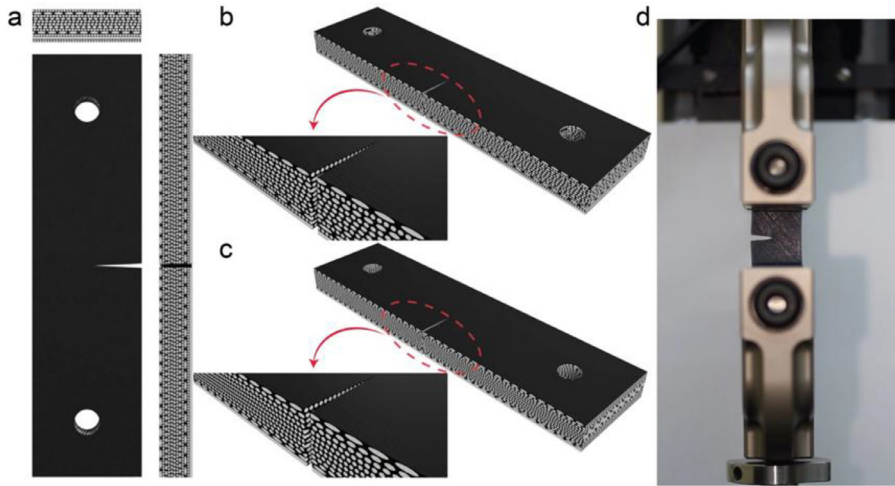
Fig. A4. Design of 3-D printing synthetic Bouligand structures. (a) A three-view drawing of double-twisted Bouligand sample. (b–c) Oblique drawing of double-twisted and single Bouligand samples. The white indicates printed fibers and black is soft matrix. (d) Mechanical testing performed on the Instron-5933 screw-driven testing machine.

As above, the phase parameter d can be solved by minimizing Eq. (A1). The analytical solution of phase-field parameter can then be written as:

$$d = \frac{2H}{\frac{G_c}{l_0} + 2H} = \frac{2\Psi_e}{\frac{G_c}{l_0} + 2\Psi_e} = \frac{\frac{2\mu}{\beta}\left((1+\epsilon_y)^{-\beta} - 1\right) + \mu\left((1+\epsilon_y)^2 - 1\right)}{\frac{G_c}{l_0} + \frac{2\mu}{\beta}\left((1+\epsilon_y)^{-\beta} - 1\right) + \mu\left((1+\epsilon_y)^2 - 1\right)}. \tag{A5}$$

The corresponding axial stress is $\sigma_y = \frac{\partial \Psi_e}{\partial \epsilon_y} = \mu(1+\epsilon_y) - \mu(1+\epsilon_y)^{-\beta-1}$, and as such, the degradation function is given by:

$$\widetilde{\sigma}_y = \left[\mu(1+\epsilon_y) - \mu(1+\epsilon_y)^{-\beta-1}\right] * \left[(1-d)^2 + k\right] \tag{A6}$$

Fig. A2a shows the axial stress computed by analytical solution (Eq. (A6)) and our current work. Fig. A2b shows the phase-field parameter d as a function of the applied strain. The black line represents the results of this work; the black circles represent the analytical solutions in Eq. (A5). Very good agreement can be found between the current implementation and analytical solution, as shown in Fig. A2.

A3. Perforated asymmetric bending test

To further validate our implementation, we performed the numerical test known as perforated asymmetric bending test (Bittencourt et al., 1996) and compared the results with previous simulation and experiment observations (Miehe et al., 2010b; Molnár and Gravouil, 2017).

To compare with literature results, a 2-D model with a hyperelastic constitutive law in finite strain is implemented by replacing the strain energy function as $\Psi_e = \frac{\mu}{\beta}(J^{-\beta} - 1) + \frac{\mu}{2}(tr(\mathbf{C}) - 2)$ in our AceGen platform; the crack-surface density function again remains the same as in Eq. (2). The user-defined element is a 2-D 4-node element. The materials and phase-field parameters are set the same as in the literature (Miehe et al., 2010b; Molnár and Gravouil, 2017): The Young's modulus of the element is set to $E = 20.8$ kN/mm^2 and the Poisson's ratio to $\nu = 0.3$. The critical energy release rate is $G_c = 0.001$ kN/mm and the length-scale parameter is $l_0 = 0.025$ mm. The anisotropic parameter α is set to be 0. Fig. A3a shows the geometry and boundary conditions of the tested asymmetric notched beam with three holes. The mesh around the holes and the initial crack are refined to be toughly $h = 0.01$ mm. Fig. A3b shows the experimental observation from Bittencourt et al. (1996). It is clear that our simulation can precisely recover the crack path, as shown in Fig. A3c.

Appendix B. Characterization, fabrication and testing of synthetic Bouligand samples

SEM observation: Arapaima and coelacanth fish scales were chosen to give the examples of single and double-twisted Bouligand structures. The fish scales were frozen in the liquid nitrogen and fractured. Samples were then fixed in a 2% glutaraldehyde solution for 3 hrs and subsequently dehydrated in 30% 50%, 70%, 90%, and 100% (three times) ethanol solutions. The samples were then dried in a critical point dryer (Tousimis Auto Samdri 815A), and the surfaces were sputter coated with iridium (Emitech K575X). A FEI SFEG ultrahigh-resolution SEM (FEI, Hillsboro) was used to visualize the arrangement of the Bouligand structure.

Tension samples, with a gauge length of 6 mm and width of 4 mm, were prepared in the longitudinal direction of the fish scales. Before testing, a ~2-mm long pre-crack was made using a new razor blade in each sample. Uniaxial tension tests were performed at 25 °C in an environmental Hitachi S-4300SE/N (Hitachi America, Pleasanton, CA) SEM. Before the sample preparation, the scales were frozen normally and kept in the aluminum foil with icy bags on 30 mins prior to testing. Testing was performed at a displacement rate of 0.5 mm·min^{-1} using a Gatan Microtest 150 N bending stage (Gatan, Abington, UK) inside the SEM.

3-D Printing: Single-edged notched tension samples of the single and double-twisted Bouligand structures were designed by Autodesk Fusion 360 (Autodesk®, San Rafael, CA) and printed using a PolyJet 3-D printer (Objet260 Connex3, Stratasys®, Eden Prairie, MN). Specimens dimensions were 100 mm (length), 26 mm (width) with a thickness of 7.8 mm, and contained an 11-mm long edge notch. The design is shown in Fig. A4a.

The 3-D printing was performed with a multi-materials set-up in order to mimic the collagen fibrils and the interfibrillar matrix in biomaterials. Two different PolyJet materials were used; one is a rigid polymer (VeroWhite, Young's modulus ~ 2000–3000 MPa, by Stratasys®) printed as collagen fibrils, the other is a soft rubber-like polymer (TangoBlackPlus, breaking strain ~ 170–220%, by Stratasys®) printed as a soft matrix. The supporting material (SUP705, an acrylic compound by Stratasys®) for 3-D printing process was removed in a solution of caustic soda and sodium metasilicate without damaging the other components after printing.

In each printed single lamella (650 μm in thickness), the collagen fibrils were printed as cylinders in a specific orientation with a 500-μm diameter (interspace is 75 μm); all the fibrils are embedded in a soft matrix, as shown in Fig. A4b-c. The synthetic Bouligand structure was composed by 12 different lamellae with specific stacking sequences. The stacking angles in single Bouligand sample were arranged as −90°, −75°, −60°, −45°, −30°, −15°, 0°, 15°, 30°, 45°, 60°, 75°, while those in double-twisted structure were 0°, −90°, 15°, −75°, 30°, −60°, 45°, −45°, 60°, −30°, 75°, −15° (the stacking angle was defined as in Fig. 6a). Note that in these 3-D printed samples, the white fibers were embedded in the black matrix as shown in Fig. A4a. The matrix is actually a continuous body and consequently does not have boundaries between different layers; it can therefore be regarded as representing the perfect bonding case in any finite simulation.

Mechanical testing: Uniaxial tensile tests were performed on a screw-driven mechanical testing machine (Instron-5933, Norwood, MA) with a 2 kN maximum load cell as shown in Fig. A1d. The specimen gauge lengths were set at 38 mm. Testing was carried out in room temperature air at a cross-head speed of 10 mm·min^{-1}.

Supplementary materials

Supplementary material associated with this article can be found, in the online version, at doi:10.1016/j.jmps.2019.07.001.

References

Al-Sawalmih, A., Li, C., Siegel, S., Fabritius, H., Yi, S., Raabe, D., Fratzl, P., Paris, O., 2008. Microtexture and chitin/calcite orientation relationship in the mineralized exoskeleton of the American lobster.. Adv. Funct. Mater. 18, 3307–3314.

Bittencourt, T., Wawrzynek, P., Ingraffea, A., Sousa, J., 1996. Quasi-automatic simulation of crack propagation for 2D LEFM problems. Eng. Fract. Mech. 55, 321–334.

Bourdin, B., Francfort, G.A., Marigo, J.-J., 2000. Numerical experiments in revisited brittle fracture. J. Mech. Phys. Solids 48, 797–826.

Bourdin, B., Francfort, G.A., Marigo, J.-J., 2008. The variational approach to fracture. J. Elast. 91, 5–148.

Bruet, B.J., Song, J., Boyce, M.C., Ortiz, C., 2008. Materials design principles of ancient fish armour. Nat. Mater. 7, 748.

Chen, I.H., Kiang, J.H., Correa, V., Lopez, M.I., Chen, P.-Y., McKittrick, J., Meyers, M.A., 2011. Armadillo armor: mechanical testing and micro-structural evaluation. J. Mech. Behav. Biomed. Mater. 4, 713–722.

Chen, I.H., Yang, W., Meyers, M.A., 2015. Leatherback sea Turtle shell: a tough and flexible biological design. Acta Biomater. 28, 2–12.

Chen, P.-Y., Lin, A.Y.-M., McKittrick, J., Meyers, M.A., 2008. Structure and mechanical properties of Crab exoskeletons. Acta Biomater. 4, 587–596.

Chen, S.-M., Gao, H.-L., Zhu, Y.-B., Yao, H.-B., Mao, L.-B., Song, Q.-Y., Xia, J., Pan, Z., He, Z., Wu, H.-A., 2018. Biomimetic twisted plywood structural materials. Natl. Sci. Rev. 5, 703–714.

Dastjerdi, A.K., Barthelat, F., 2015. Teleost fish scales amongst the toughest collagenous materials. J. Mech. Behav. Biomed. Mater. 52, 95–107.

Dennell, R., 1974. The cuticle of the crabs cancer pagurus L. and carcinus maenas (L.). Zool. J. Linn. Soc. 54, 241–245.

Feilden, E., Ferraro, C., Zhang, Q., García-Tuñón, E., D'elia, E., Giuliani, F., Vandeperre, L., Saiz, E., 2017. 3D printing bioinspired ceramic composites. Sci. Rep. 7, 13759.

Fischer, F., Kolednik, O., Predan, J., Razi, H., Fratzl, P., 2017. Crack driving force in twisted plywood structures. Acta Biomater. 55, 349–359.

Francfort, G.A., Marigo, J.-J., 1998. Revisiting brittle fracture as an energy minimization problem. J. Mech. Phys. Solids 46, 1319–1342.

Giraud, M., Castanet, J., Meunier, F., Bouligand, Y., 1978. The fibrous structure of coelacanth scales: a twisted 'plywood'. Tissue and Cell 10, 671–686.

Guarín-Zapata, N., Gomez, J., Yaraghi, N., Kisailus, D., Zavattieri, P.D., 2015. Shear wave filtering in naturally-occurring Bouligand structures. Acta Biomater. 23, 11–20.

Gültekin, O., Dal, H., Holzapfel, G.A., 2018. Numerical aspects of anisotropic failure in soft biological tissues favor energy-based criteria: a rate-dependent anisotropic crack phase-field model. Comput. Methods Appl. Mech. Eng. 331, 23–52.

Itskov, M., Aksel, N., 2004. A class of orthotropic and transversely isotropic hyperelastic constitutive models based on a polyconvex strain energy function. Int. J. Solids Struct. 41, 3833–3848.

Korelc, J., 2002. Multi-language and multi-environment generation of nonlinear finite element codes. Eng. Comput. 18, 312–327.

Li, B., Peco, C., Millán, D., Arias, I., Arroyo, M., 2015. Phase-field modeling and simulation of fracture in brittle materials with strongly anisotropic surface energy. Int. J. Numer. Methods Eng. 102, 711–727.

Ling, S., Kaplan, D.L., Buehler, M.J., 2018. Nanofibrils in nature and materials engineering.. Nature Rev. Mater. 3, 18016.

Mao, Y., Anand, L., 2018. A theory for fracture of polymeric gels. J. Mech. Phys. Solids 115, 30–53.

Mao, Y., Talamini, B., Anand, L., 2017. Rupture of polymers by chain scission. Extreme Mech. Lett. 13, 17–24.

Miehe, C., Dal, H., Schänzel, L.M., Raina, A., 2016. A phase-field model for chemo-mechanical induced fracture in lithium-ion battery electrode particles. Int. J. Numer. Methods Eng. 106, 683–711.

Miehe, C., Hofacker, M., Welschinger, F., 2010a. A phase field model for rate-independent crack propagation: robust algorithmic implementation based on operator splits. Comput. Methods Appl. Mech. Eng. 199, 2765–2778.

Miehe, C., Schaenzel, L.-M., Ulmer, H., 2015. Phase field modeling of fracture in multi-physics problems. Part I. Balance of crack surface and failure criteria for brittle crack propagation in thermo-elastic solids. Comput. Methods Appl. Mech. Eng. Fract. Mech. 294, 449–485.

Miehe, C., Schänzel, L.-M., 2014. Phase field modeling of fracture in rubbery polymers. Part I: finite elasticity coupled with brittle failure. J. Mech. Phys. Solids 65, 93–113.

Miehe, C., Welschinger, F., Hofacker, M., 2010b. Thermodynamically consistent phase-field models of fracture: variational principles and multi-field FE implementations. Int. J. Numer. Methods Eng. 83, 1273–1311.

Molnár, G., Gravouil, A., 2017. 2D and 3D abaqus implementation of a robust staggered phase-field solution for modeling brittle fracture. Finite Elem. Anal. Des. 130, 27–38.

Murcia, S., Lavoie, E., Linley, T., Devaraj, A., Ossa, E.A., Arola, D., 2017. The natural armors of fish: a comparison of the lamination pattern and structure of scales. J. Mech. Behav. Biomed. Mater. 73, 17–27.

Quan, H., Yang, W., Schaible, E., Ritchie, R.O., Meyers, M.A., 2018. Novel defense mechanisms in the armor of the scales of the "living fossil" coelacanth fish. Adv. Funct. Mater., 1804237.

Raabe, D., Sachs, C., 2005. Mechanical properties of the lobster cuticle. MRS Online Proceedings Library Archive 874.

Raina, A., Miehe, C., 2016. A phase-field model for fracture in biological tissues. Biomech. Modeling Mechanobiol. 15, 479–496.

Sachs, C., Fabritius, H., Raabe, D., 2006. Experimental investigation of the elastic–plastic deformation of mineralized lobster cuticle by digital image correlation. J. Struct. Biol. 155, 409–425.

Schröder, J., Neff, P., 2003. Invariant formulation of hyperelastic transverse isotropy based on polyconvex free energy functions. Int. J. Solids Struct. 40, 401–445.

Schröder, J., Neff, P., Ebbing, V., 2008. Anisotropic polyconvex energies on the basis of crystallographic motivated structural tensors. J. Mech. Phys. Solids 56, 3486–3506.

Sherman, V.R., Yang, W., Meyers, M.A., 2015. The materials science of collagen. J. Mech. Behav. Biomed. 52, 22–50.

Shin, Y.A., Yin, S., Li, X., Lee, S., Moon, S., Jeong, J., Kwon, M., Yoo, S.J., Kim, Y.-M., Zhang, T., Gao, H., Oh, S.H., 2016. Nanotwin-governed toughening mechanism in hierarchically structured biological materials.. Nat. Commun. 7.

Suksangpanya, N., Yaraghi, N.A., Kisailus, D., Zavattieri, P., 2017. Twisting cracks in Bouligand structures. J. Mech. Behav. Biomed. Mater. 76, 38–57.

Suksangpanya, N., Yaraghi, N.A., Pipes, R.B., Kisailus, D., Zavattieri, P., 2018. Crack twisting and toughening strategies in Bouligand architectures. Int. J. Solids Struct. 150, 83–106.

Szczesny, S.E., Elliott, D.M., 2014. Interfibrillar shear stress is the loading mechanism of collagen fibrils in tendon. Acta Biomater. 10, 2582–2590.

Tadayon, M., Amini, S., Masic, A., Miserez, A., 2015. The mantis shrimp saddle: a biological spring combining stiffness and flexibility. Adv. Funct. Mater. 25, 6437–6447.

Teichtmeister, S., Kienle, D., Aldakheel, F., Keip, M.-A., 2017. Phase field modeling of fracture in anisotropic brittle solids. Int. J. Non Linear Mech. 97, 1–21.

Torres, F., Malásquez, M., Troncoso, O., 2015. Impact and fracture analysis of fish scales from arapaima gigas. Mater. Sci. Eng. 51, 153–157.

Velasco-Hogan, A., Xu, J., Meyers, M.A., 2018. Additive manufacturing as a method to design and optimize bioinspired structures. Adv. Mater. 30, 1800940.

Wagner, D.O., Aspenberg, P., 2011. Where did bone come from? An overview of its evolution. Acta Orthop. 82, 393–398.

Wu, W., Owino, J., Al-Ostaz, A., Cai, L., 2014. Applying periodic boundary conditions in finite element analysis. In: SIMULIA Community Conference, Providence, pp. 707–719.

Xu, X.-P., Needleman, A., 1994. Numerical simulations of fast crack growth in brittle solids. J. Mech. Phys. Solids 42, 1397–1434.

Yang, R., Zaheri, A., Gao, W., Hayashi, C., Espinosa, H.D., 2017a. AFM identification of beetle exocuticle: Bouligand structure and nanofiber anisotropic elastic properties. Adv. Funct. Mater. 27, 1603993.

Yang, W., Chen, I.H., Gludovatz, B., Zimmermann, E.A., Ritchie, R.O., Meyers, M.A., 2013a. Natural flexible dermal armor. Adv. Mater. 25, 31–48.

Yang, W., Gludovatz, B., Zimmermann, E.A., Bale, H.A., Ritchie, R.O., Meyers, M.A., 2013b. Structure and fracture resistance of alligator gar (Atractosteus spatula) armored fish scales. Acta Biomater. 9, 5876–5889.

Yang, W., Naleway, S.E., Porter, M.M., Meyers, M.A., McKittrick, J., 2015. The armored carapace of the boxfish. Acta Biomater. 23, 1–10.

Yang, W., Sherman, V.R., Gludovatz, B., Mackey, M., Zimmermann, E.A., Chang, E.H., Schaible, E., Qin, Z., Buehler, M.J., Ritchie, R.O., 2014. Protective role of arapaima gigas fish scales: structure and mechanical behavior. Acta Biomater. 10, 3599–3614.

Yang, Y., Chen, Z., Song, X., Zhang, Z., Zhang, J., Shung, K.K., Zhou, Q., Chen, Y., 2017b. Biomimetic anisotropic reinforcement architectures by electrically assisted nanocomposite 3D printing. Adv. Mater. 29, 1605750.

Zaheri, A., Fenner, J.S., Russell, B.P., Restrepo, D., Daly, M., Wang, D., Hayashi, C., Meyers, M.A., Zavattieri, P.D., Espinosa, H.D., 2018. Revealing the mechanics of helicoidal composites through additive manufacturing and beetle developmental stage analysis. Adv. Funct. Mater. 28, 1803073.

Zhu, D., Ortega, C.F., Motamedi, R., Szewciw, L., Vernerey, F., Barthelat, F., 2012. Structure and mechanical performance of a "modern" fish scale. Adv. Eng. Mater. 14, B185–B194.

Zhu, D., Szewciw, L., Vernerey, F., Barthelat, F., 2013. Puncture resistance of the scaled skin from striped bass: collective mechanisms and inspiration for new flexible armor designs. J. Mech. Behav. Biomed. Mater. 24, 30–40.

Zimmermann, E.A., Gludovatz, B., Schaible, E., Dave, N.K., Yang, W., Meyers, M.A., Ritchie, R.O., 2013. Mechanical adaptability of the Bouligand-type structure in natural dermal armour. Nat. Commun. 4, 2634.